JOURNAL OF THE AMERICAN CHEMICAL SOCIETY

pubs.acs.org/JACS

Article

Amphoteric Behavior of Hydrogen in Lanthanum Oxyhydrides: Correlation with Electrochemical Properties

Tomoyuki Yamasaki,* Keiga Fukui, Soshi Iimura, Shunsuke Tsuda, Hiroshi Mizoguchi, Takahisa Omata, and Hideo Hosono

Cite This: *J. Am. Chem. Soc.* 2026, 148, 11393−11402

Read Online

ACCESS | Metrics & More | Article Recommendations | Supporting Information

ABSTRACT: Hydrogen incorporated into solids can adopt either protonic (H^+) or hydridic (H^-) characteristics depending on the position of the Fermi level of the host material. In recent years, not only proton-conducting materials but also hydride-ion-conducting materials have been actively developed, enabling the development of novel electrochemical devices that exploit the amphoteric nature of hydrogen. At present, however, the relationship between the electrochemical properties of hydrogen-ion-conducting materials and the amphoteric nature of hydrogen remains scarcely explored. Herein, we investigate the electrochemical window (ECW) of the H^- conductor $LaH_{3-2x}O_x$ and elucidate the underlying amphoteric behavior of hydrogen. We determine the band alignment of $LaH_{3-2x}O_x$ and map the ECW onto an electronic energy scale referenced to the vacuum level. Based on this band alignment, we examine the conduction behavior of $LaH_{3-2x}O_x$ in a H_2 atmosphere via electromotive force measurements of a hydrogen concentration cell. The reducing limit of the ECW was governed by hydrogen extraction from $LaH_{3-2x}O_x$, whereas its oxidizing limit was governed by the capture of positive charge by interstitial H^-, leading to H^+ formation and electronic conduction. Electromotive force measurements of a hydrogen concentration cell revealed that, in addition to H^- conduction, a finite contribution from H^+ conduction emerges near a hydrogen partial pressure of 1 atm. By capturing the amphoteric nature of hydrogen on an electronic energy scale, this paper provides a unified perspective across different classes of hydrogen-ion conductors.

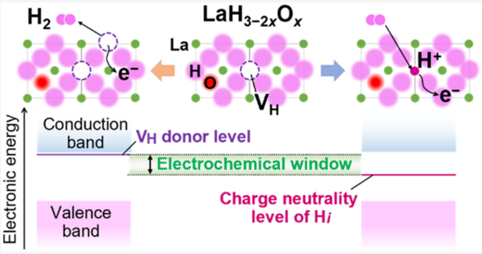

INTRODUCTION

Hydrogen in solids exhibits various bonding motifs and charge states, ranging from protonic (H^+) to hydridic (H^-). This amphoteric nature governs various material properties such as charge-carrier transport, magnetic behavior, and chemical reactivity.[1−8] Hydrogen-ion-conducting materials, including both H^+ and H^- conductors, have been actively developed as key components for fuel cells and other electrochemical energy conversion and storage devices.[9−18] Along with the development of materials exhibiting high ionic conductivity, investigations on the characteristic features of hydrogen ions in solids beyond mere differences in charge polarity, such as their distinct chemical reactivity and reaction selectivity, have also increased.[19−21] The availability of a unified descriptor that captures these properties of hydrogen in solids would contribute to the rational design of new functional materials and electrochemical devices, thereby opening up new possibilities of hydrogen-based ionics.

In semiconductors, hydrogen often occupies interstitial sites in the host semiconductor lattice, where it can act as a donor or acceptor upon ionization into H^+ or H^-, thereby altering the electrical conductivity of the host material.[22,23] Hydrogen charge states and donor/acceptor behaviors are often discussed in terms of the theoretically calculated energies of interstitial-hydrogen defect levels within band alignments referenced to the vacuum level ($E_{vac.}$) to understand their impact on charge transport in semiconductors.[24,25] The validity of this concept has been corroborated experimentally, for example, by muon spin spectroscopy.[26,27]

Recently, conceptual frameworks that consider electronic structure and band-edge positions, established in semiconductor materials and device research, have increasingly been extended to the design of electrochemical devices employing ion conductors. In Li-ion battery applications, for example, the band alignments of Li-conducting materials have emerged as powerful tools for the design of electrolytes with a wide electrochemical window (ECW)[28,29]—the potential range over which an electrolyte functions without electronic leakage—and for optimizing electrode/electrolyte interfaces.[30,31]

By contrast, the electrochemical characteristics of hydrogen-ion-conducting materials have not yet been viewed from an electronic energy scale referenced to the $E_{vac.}$, which is

Received: January 26, 2026
Revised: February 26, 2026
Accepted: February 27, 2026
Published: March 6, 2026

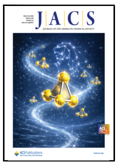

https://doi.org/10.1021/jacs.6c01849

commonly used in semiconductor research. One reason is that the applications of conventional proton-conducting materials have been largely confined to fuel cells and steam electrolysis cells, where the operating potential range is constrained by the H^+/H_2 and O_2/H_2O redox couples. However, recent progress in H^- conductors is changing this landscape. It has been shown that proton-conducting In-doped $BaZrO_3$, when exposed to strongly reducing atmospheres, undergoes hydrogen reduction to form H^-, thereby exhibiting mixed H^- and electron conduction.[18,32] In addition, electrolytic devices that integrate proton-conducting and hydride-ion-conducting In-doped $BaZrO_3$ phases have been demonstrated.[33] For the design of new electrochemical devices that exploit hydrogen amphoteric behavior, it is essential to describe the redox properties of hydrogen from the viewpoint of electronic energy scale.

In this study, we focus on lanthanum oxyhydrides, $LaH_{3-2x}O_x$, which are H^- conductors exhibiting fast H^- diffusivity.[34,35] This class of materials is regarded as a highly promising candidate for realizing new electrochemical devices for CO_2 reduction and NH_3 synthesis by leveraging the high reducing ability of H^-.[36,37] Herein, we reveal the amphoteric behavior of hydrogen in $LaH_{3-2x}O_x$ under hydrogen atmospheres that are oxidizing conditions for H^-. We further show that partial protonation of hydrogen under these conditions defines the ECW of $LaH_{3-2x}O_x$, which is rationalized by an energy band alignment obtained from photoemission experiments and defect levels estimated by first-principles calculations.

EXPERIMENTAL SECTION

Synthesis of Sintered $LaH_{3-2x}O_x$ Pellets

Sintered $LaH_{3-2x}O_x$ pellets were prepared for the electrical measurements. LaH_3 powder was obtained by hydrogenating La ingots (99.9%, Rare Metallic Co., Ltd.) via annealing at 400 °C under a ~1 MPa H_2 atmosphere for 10 h. The resulting LaH_3 powder was mixed with La_2O_3 (99.9%, Kojundo Chemical Laboratory Co., Ltd.) using a zirconia mortar and pestle inside an Ar-filled glovebox. The mixed powders were subsequently annealed at 775 °C under vacuum to obtain $LaH_{3-2x}O_x$. During this process, LaH_3 was dehydrogenated to a metallic La, which promoted powder sintering. The samples were rehydrogenated under a hydrogen atmosphere. Subsequent slow cooling yielded crack-free H^--conductive pellets. Structural characterization was performed via X-ray diffraction (Rigaku Corp. MiniFlex600) in an airtight capsule. Lattice parameters were determined by Rietveld analysis using SmartLab Studio II (Rigaku Corp.). The dependence of the lattice parameters of $LaH_{3-2x}O_x$ on its oxygen content agreed with the results reported in an earlier work (Figure S1).[34] The obtained compositions were consistent with the nominal molar ratio of LaH_3 and La_2O_3, indicating that oxygen contamination during synthesis was negligible. The sintered $LaH_{3-2x}O_x$ pellets were dense, with relative densities exceeding 95%, as confirmed by cross-sectional microscopic observations (Figure S2).

Preparation of $LaH_{2.8}O_{0.1}$ Thin Films

$LaH_{2.8}O_{0.1}$ thin films were deposited at room temperature by radio frequency (RF) magnetron sputtering (Kenix Co., Ltd.) with 2-in. La metal targets (99.9%, Rare Metallic Co., Ltd.). The chamber pressure was pumped down to 5×10^{-5} Pa prior to deposition. Deposition was performed in flowing Ar (99.9999%) with 12.5 vol % H_2 (99.99999%). The deposition pressure was maintained at 0.6 Pa. The as-deposited films were hydrogen-deficient and, hence, metallic. Immediately after deposition and without air exposure, the films were exposed to pure H_2 gas at room temperature to dose hydrogen and achieve an electronically insulating state (Figure S3). The apparent stoichiometric composition of the films was estimated by comparing the optical band gap determined from the transmission measurements with that of powder samples synthesized by a solid-state reaction, the details of which are described elsewhere.[38] Although oxygen was not intentionally introduced during deposition, the resulting films exhibited oxygen incorporation, likely owing to the presence of residual oxygen- and/or water-related species in the sputtering chamber.

Electrical Measurements

Prior to the electrical measurements of the sintered $LaH_{2.8}O_{0.1}$ samples (6 mm in diameter and approximately 1 mm in thickness), 200 nm Mo or 50 nm Pd electrodes were deposited onto both sides of the pellets by RF magnetron sputtering. The $LaH_{2.8}O_{0.1}$ sample was placed on a homemade test jig in an airtight chamber. Alternating-current (AC) impedance spectroscopy was performed from −100 to 100 °C under flowing N_2 or H_2 at ambient pressure, and the bulk $LaH_{2.8}O_{0.1}$ and electrode interfacial resistances were extracted. Spectra were recorded from 10 MHz to 1 mHz with an oscillation amplitude of 100 mV using impedance analyzers (Solartron SI 1260 or Novocontrol α-A equipped with a ZG2 interface). For the $LaH_{2.8}O_{0.1}$ thin films, a capacitor-like cell, $Pd/LaH_{2.8}O_{0.1}/Mo$, was fabricated on a Si wafer. The $LaH_{2.8}O_{0.1}$ layer thickness was 500 nm. A 50 nm Pd top electrode (5 mm in diameter) and 100 nm Mo bottom electrode were also deposited by RF magnetron sputtering. Sweep voltammetry was performed by using a potentiostat−galvanostat (Solartron SI 1287A) at 25 °C under a H_2 atmosphere with a scan rate of 1 mV s^{-1}.

Electromotive Force (EMF) Measurements of a Hydrogen Concentration Cell

EMF measurements were performed using a symmetric $Pd/LaH_{2.8}O_{0.1}/Pd$ cell over 25−100 °C. The pellet was mounted on the tube-end face, and its periphery was sealed with heat-resistant epoxy to separate the atmospheres on the two faces. A small hydrogen partial-pressure difference was applied, and the EMF was recorded with a potentiostat (Solartron SI 1287A).

Ultraviolet Photoelectron Spectroscopy (UPS)

UPS measurements were conducted in a vacuum chamber with a base pressure below 5×10^{-8} Pa by irradiation with He I emission lines (21.22 eV). The emitted photoelectrons were detected using a hemispherical analyzer (Scienta Omicron DA30-L) with a 10 eV pass energy. Because UPS is highly sensitive to surface contamination, the $LaH_{3-2x}O_x$ pellets were fractured in a preparation chamber (~7×10^{-8} Pa) immediately before measurement. Secondary-electron cutoff spectra were acquired under a negative sample bias to determine the position of the vacuum level E_{vac}.

Photoelectron Yield Spectroscopy (PYS)

PYS was carried out with monochromated photons (2.0−4.8 eV) from a Xe lamp (Asahi Spectra MAX-303). The photon flux was calibrated with an optical power detector (Newport 818-UV). A −50 V bias was applied to the sample to extract photoelectrons, and the resulting current to ground was recorded with a pico-ammeter (Keithley 6482).

Inverse Photoelectron Spectroscopy (IPES)

IPES measurements were conducted in bremsstrahlung isochromat spectroscopy (BIS) mode, using an IPES system (PSP Vacuum Technology, Ltd.). Immediately before each measurement, a sintered pellet was scraped inside the vacuum chamber to achieve a clean surface. The kinetic energy of incident electrons was scanned from 5 to 20 eV, and emitted photons were detected with a bandpass detector comprising a fluoride window and a NaCl-coated Ta cone. The energy scale was calibrated by measuring the Fermi edge of Au foil, thereby determining the instrumental Fermi level (E_F).

Density Functional Theory (DFT) Calculations

Periodic DFT calculations were performed as implemented in the VASP code.[39,40] The exchange and correlation energies were calculated by generalized gradient approximation using Perdew−Burke−Ernzerhof parametrization.[41] Valence electrons were expanded

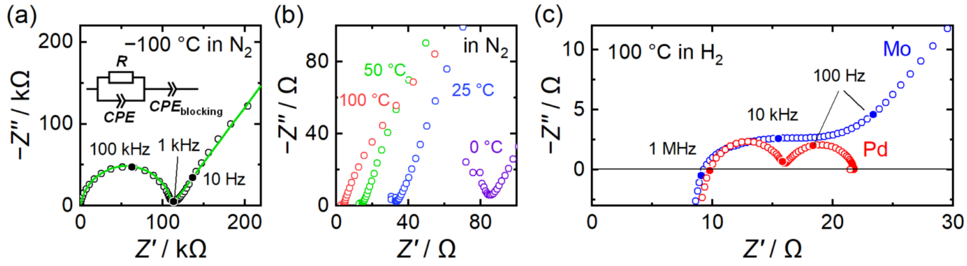

Figure 1. Nyquist plots of a sintered $LaH_{2.8}O_{0.1}$ pellet. (a) Nyquist plot measured with Mo electrodes at −100 °C under a N_2 atmosphere. The green line represents the fitting result obtained using an equivalent circuit consisting of a resistor, *R*, and constant phase elements, *CPEs*, connected in parallel along with an additional *CPE* accounting for ion-blocking polarization. (b) Temperature dependence of the Nyquist plots measured with Mo electrodes under a N_2 atmosphere. The purple, blue, green, and red open circles correspond to temperatures of 0, 25, 50, and 100 °C, respectively. (c) Nyquist plots measured at 100 °C under a H_2 atmosphere. The blue and red open circles represent data obtained with Mo (ion-blocking) and Pd (ion-reversible) electrodes, respectively.

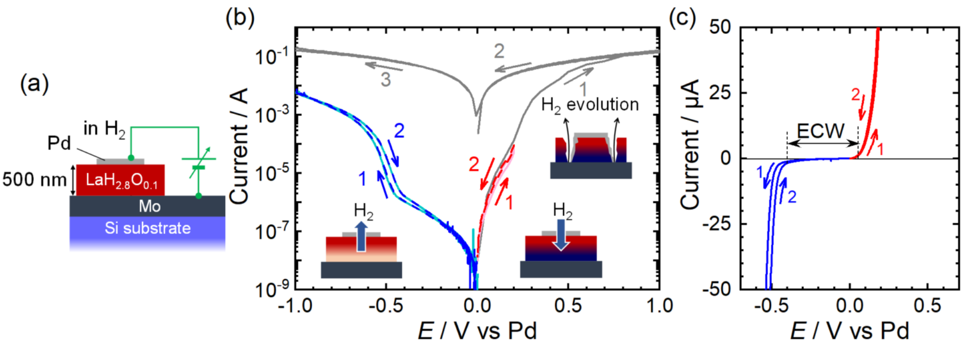

Figure 2. Measurement of the ECW of a $LaH_{2.8}O_{0.1}$ thin film. (a) Schematic illustration of an asymmetric Pd/$LaH_{2.8}O_{0.1}$/Mo electrochemical cell fabricated on a Si substrate. A DC bias was applied to the cell under 1 atm H_2. The Pd electrode was taken to be in equilibrium with hydrogen and was used as a nonpolarizable reference electrode. (b, c) *I*−*V* curves obtained by linear sweep voltammetry of the cell shown in (a) at a scan rate of 1 mV s^{-1} plotted on a (b) logarithmic and (c) linear current scale. A cathodic polarization was applied to the Mo electrode with respect to the Pd electrode by sweeping the potential in the range 0 V → −1 V → 0 V vs Pd, extracting hydrogen from the thin film. The first and second cycles are shown in sky blue and blue, respectively. An anodic polarization was applied by sweeping the potential in the range 0 V → 0.2 V → 0 V vs Pd, injecting hydrogen into the thin film. The first and second cycles are shown in pink and red, respectively. The *I*−*V* curves measured under potentials above 0.2 V are shown in gray. After a current kink at approximately 0.2 V, the film becomes irreversibly low-resistive, which is attributed to H_2 evolution at the bottom Mo electrode and the destruction of the capacitor-like structure.

in terms of a plane wave basis set, with the core electrons treated using the projected augmented wave approach.[42] The plane wave cutoff energy was set to 520 eV for all systems, and the Brillouin zone was sampled with a *k*-point grid with a spacing of 0.03 × 2*π* $Å^{-1}$. The convergence threshold was set to 1.0 × 10^{-8} eV for electronic relaxation and 2.0 × 10^{-5} eV $Å^{-1}$ for force relaxation. A 2 × 2 × 2 supercell of $LaH_{2.5}O_{0.25}$ with $R\bar{3}m$ symmetry[43] (containing 120 atoms) was constructed to evaluate the defect behavior. The pydefect code[44] was used to handle and analyze the defect calculations.

■ RESULTS AND DISCUSSION

Figure 1a,b show Nyquist plots of the AC impedance for a sintered $LaH_{2.8}O_{0.1}$ pellet measured using Mo electrodes between −100 and 100 °C under a N_2 atmosphere. At lower temperatures, a nearly ideal semicircle appears in the high-frequency region, which is attributed to bulk hydride-ion transport in $LaH_{2.8}O_{0.1}$. This indicates that the contribution from grain-boundary conduction is negligibly small, which is consistent with the high relative density of the sintered sample and the smooth fracture surface observed in Figure S2. The linear impedance response observed in the low-frequency region reflects negligible electronic conduction in $LaH_{2.8}O_{0.1}$ and strongly hindered hydrogen transport at the Mo/$LaH_{2.8}O_{0.1}$ interface, giving rise to a diffusion-limited response with pronounced resistive and capacitive components. These results confirm the ion-blocking nature of the Mo electrode. As the temperature increases, the semicircle in the high-frequency region gradually disappears, leaving only a resistive component. This behavior indicates that ionic transport in the bulk becomes fast with increasing temperature so that its capacitive contribution can no longer be resolved within the measured frequency range. Ionic conductivity was estimated from the bulk response, which was fitted with an equivalent circuit consisting of a resistor (*R*) and constant-phase elements (*CPEs*) connected in parallel for lower temperatures or with a single resistor for higher temperatures. The electronic conductivity of $LaH_{2.8}O_{0.1}$ was subsequently determined from the steady-state current under an applied direct-current (DC) bias in this ion-blocking cell (Figure S4). The obtained ionic and electronic conductivities agree well with previously reported values for $LaH_{2.8}O_{0.1}$ (Figure S5).[35] The electronic conductivity is several orders of magnitude lower than the ionic conductivity, thereby confirming that $LaH_{2.8}O_{0.1}$ behaves as an ionic conductor with an ionic transport number t_{ion} of 1.

Figure 1c shows the impedance spectra of a sintered $LaH_{2.8}O_{0.1}$ pellet measured at 100 °C under a H_2 atmosphere. When Pd electrodes, which are catalytically active for hydrogen and show hydrogen permeability,[45,46] are used, the impedance spectra (red circles) exhibit an inductive feature above 1 MHz, followed by two semicircles that converge toward the real axis at low frequencies. These semicircles are likely associated with

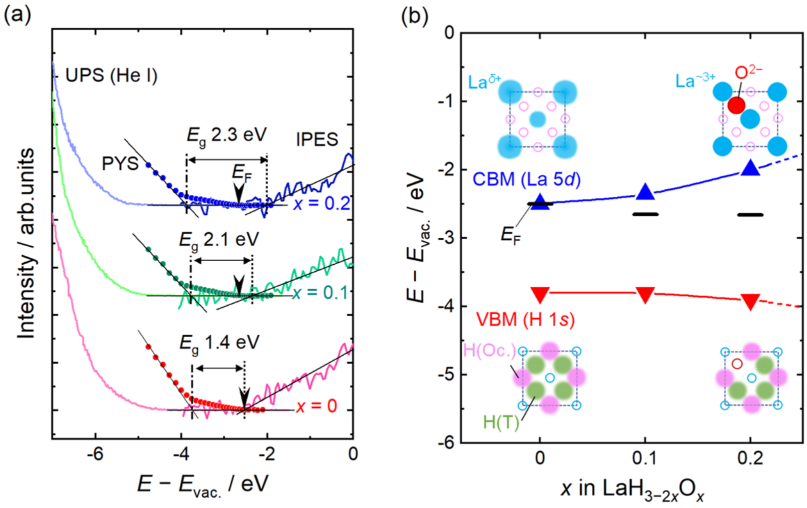

Figure 3. Energy band alignment for $LaH_{3-2x}O_x$. (a) UPS and IPES spectra (solid lines) and PYS data (dots) for $LaH_{3-2x}O_x$. All energy levels are referenced to the vacuum level ($E_{vac.}$). The spectra for $x = 0$, 0.1, and 0.2 are shown in red, green, and blue, respectively. The CBM and VBM are represented by dotted and chain lines, respectively, and E_F is marked with a black arrow. (b) Oxygen-content dependence of the CBM and VBM energies of $LaH_{3-2x}O_x$. The CBM and VBM are represented by blue and red triangles, respectively, and the corresponding E_F values are shown as black solid lines. Schematic illustrations of the arrangements of La and H atoms primarily comprising each band edge, viewed along the [100] direction, are also given.

charge-transfer reactions at the Pd interface and changes in the surface coverage of adsorbed hydrogen species.[47] Replacing Pd with Mo on the same specimen leaves the high-frequency response essentially unchanged; by contrast, in the low-frequency region, the impedance measured with Mo electrodes shows a linear response characteristic of ion-blocking (blue circles). These results indicate that Pd electrodes do not induce additional electronic conduction in $LaH_{2.8}O_{0.1}$, but enable ion transport across the Pd/$LaH_{2.8}O_{0.1}$ interfaces and act as ion-reversible electrodes.

Figure 2a shows a schematic illustration of an asymmetric Pd/$LaH_{2.8}O_{0.1}$/Mo cell fabricated on a Si substrate. The asymmetric cell was polarized under a H_2 atmosphere to investigate the ECW of $LaH_{2.8}O_{0.1}$. Because hydrogen can be reversibly exchanged between the gas phase and the Pd electrode, the hydrogen chemical potential μ_H° at the Pd/$LaH_{2.8}O_{0.1}$ interface is fixed. Under a zero net H^- current (Hebb−Wagner condition),[48] the applied bias determines the hydrogen chemical potential μ_H at the Mo side, as described in eq 1.

$$\mu_H = \mu_H^\circ + \frac{RT}{2}\ln(p_{H_2}/p_{H_2}^\circ) = \mu_H^\circ + FE \tag{1}$$

where R, T, p_{H_2}, $p_{H_2}^\circ$, F, and E denote the gas constant, absolute temperature, hydrogen partial pressure at the Mo/$LaH_{2.8}O_{0.1}$ interface, hydrogen partial pressure at the Pd/$LaH_{2.8}O_{0.1}$ interface (1 atm), Faraday constant, and electric potential applied to Mo relative to Pd, respectively. Figure 2b,c show the current−voltage ($I-V$) curves obtained from the linear sweep voltammograms of the asymmetric cell measured at 25 °C. Upon the cathodic polarization of the Mo side (i.e., decreasing μ_H at the Mo/$LaH_{2.8}O_{0.1}$ interface), the current rises sharply at around −0.4 V. This onset is attributed to hydrogen release from $LaH_{3-2x}O_x$ through the Pd electrode, accompanied by the formation of hydrogen vacancies and electrons at the Mo side, according to eq 2.

$$H_H^\times \rightarrow \frac{1}{2}H_2 + V_H^\bullet + e' \tag{2}$$

where the defects are denoted according to the Kröger−Vink notation.[49] Since the hydrogen vacancies $V_H^\times$ act as shallow donors, an increase in their density leads to spatial overlap of the associated electronic states, resulting in the formation of a defect band near the conduction band minimum (CBM).[38,50] This steep increase in current indicates that electronic conduction prevails over ionic conduction in $LaH_{2.8}O_{0.1}$, which is defined as the reduction limit of the ECW of $LaH_{2.8}O_{0.1}$ (blue curve in Figure 2c). When the electric potential is swept back to values more positive than −0.4 V, the current retraces nearly the same curve as in the forward sweep, and $LaH_{2.8}O_{0.1}$ returns to a high-resistance state. Because hydrogen is incorporated into $LaH_{2.8}O_{0.1}$ through the top Pd electrode, this behavior is attributed to the refilling of hydrogen vacancies and the accompanying decrease in electron carrier density.

Conversely, under anodic polarization (i.e., increasing μ_H at the Mo/$LaH_{2.8}O_{0.1}$ interface), the current increases from ~0 V, again indicating the appearance of electronic conduction. This behavior defines the oxidation limit of the ECW of $LaH_{2.8}O_{0.1}$ (Figure 2c). When H^- ions are driven toward the bottom Mo electrode by the applied field, H_2 evolution at the Mo electrode may generate the resulting electronic current. Once the applied voltage exceeds approximately 0.2 V, the current begins to rise steeply, and, in the reverse sweep, it no longer retraces the forward curve, indicating the occurrence of an irreversible change in the cell (gray curve in Figure 2b). This trend is ascribed to an electrical short between the top and bottom electrodes caused by the destruction of the capacitor-like structure owing to H_2 evolution at the Mo electrode, as shown in Figure S6. Thus, the overpotential for the H_2 evolution reaction at the Mo electrode is estimated to be around 0.2 V. Below this overpotential, where H_2 evolution does not occur, the current in the reverse sweep retraces the forward $I-V$ curve, and this behavior remains unchanged even after repeated cycling (red curve). Thus, the increase in current

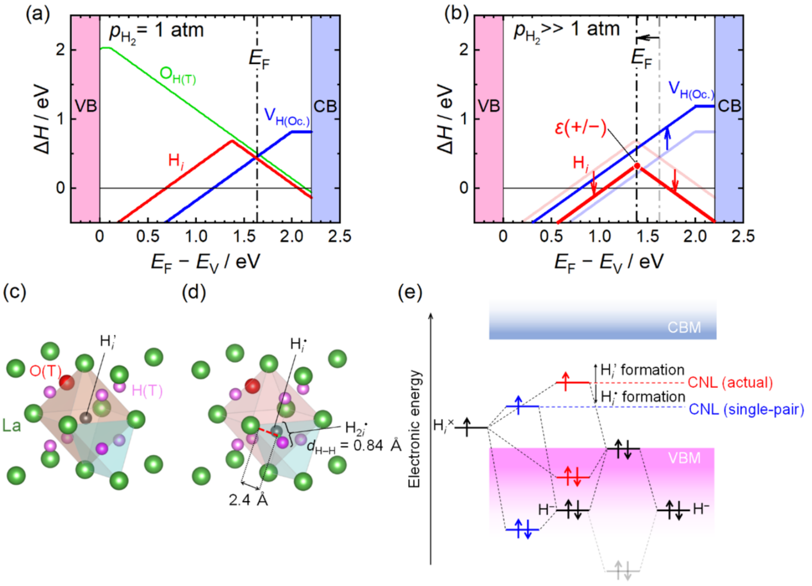

Figure 4. Calculated defect and equilibrium Fermi levels in $LaH_{2.5}O_{0.25}$. (a) Plots of the formation enthalpies (ΔH) of point defects in $LaH_{2.5}O_{0.25}$ as a function of the E_F position relative to the energy of VBM (E_V), calculated for (a) p_{H_2} = 1 atm. (b) Hypothetical plot for $p_{H_2} \gg 1$ atm at 300 K. The formation enthalpies calculated at p_{H_2} = 1 atm are shown as faint lines for comparison. H_i, $V_{H(Oc.)}$, and $O_{H(T)}$ denote an interstitial hydrogen occupying a vacant octahedral site (Oc.) created for charge compensation upon O doping, a hydrogen vacancy at an Oc. site, and an oxygen at a tetrahedral hydrogen site (T), respectively. The ε (±) represents the charge-neutrality level (CNL) of H_i. Relaxed structure upon the formation of (c) H_i' and (d) $H_i^\bullet$ in $LaH_{2.5}O_{0.25}$. La, O(T), H(T), and H_i are shown as green, red, pink, and black spheres, respectively. A dihydrogen defect is formed between $H_i^\bullet$ and a neighboring H(T), and its side-on interaction with an adjacent La atom is indicated by red dashed lines. (e) Schematic illustration of the bonding/antibonding interactions between $H_i^\times$ and a surrounding H^-, accounting for the upward shift of the CNL.

observed in this voltage range is attributed to the resistive change of $LaH_{2.8}O_{0.1}$ associated with the onset of electronic conduction. The appearance of electronic conduction when hydrogen is injected into the film under anodic polarization can be explained by two possible scenarios: (i) injected interstitial hydrogen is ionized into H^-, releasing holes

$$\frac{1}{2}H_2 \rightarrow H_i^\times \rightarrow H_i' + h^\bullet \tag{3}$$

or (ii) interstitial hydrogen is protonated and acts as an electron donor

$$\frac{1}{2}H_2 \rightarrow H_i^\times \rightarrow H_i^\bullet + e' \tag{4}$$

We investigated the origin of electronic conduction in $LaH_{3-2x}O_x$ by hydrogen injection based on the band alignment determined from the photoemission experiments and the defect energy levels evaluated by DFT calculations. Figure 3a presents the combined UPS and IPES spectra for $LaH_{3-2x}O_x$ (x = 0, 0.1, and 0.2), showing the energies of the valence band maximum (VBM), CBM, and E_F referenced to the $E_{vac.}$ and the optical band gap (E_g). The E_F were determined from the secondary-electron cutoff in the He I (21.22 eV) UPS spectra. As shown in previous work, the VBM energy of LaH_3 cannot be reliably determined from the photoemission spectra obtained by irradiation with vacuum ultraviolet (VUV) rays because the VBM is mainly composed of H 1s states with a very small density of states, and the H-1s photoionization cross section in the VUV range is small, resulting in an extremely weak photoemission intensity near the VBM.[51] Accordingly, the VBM energies for the oxyhydrides were determined from the onset of the total PYS profiles obtained by excitation with photons in the visible-to-ultraviolet light range (2.0−4.8 eV), in which the photoionization cross section of H 1s states is relatively large.[52] The resulting PYS are plotted as dots in Figure 3a. The CBM energies were determined by adding the E_g reported in an earlier study[38] to the VBM energies determined from PYS. The resulting CBMs are in good agreement with the onset of the IPES spectra.

Figure 3b shows the oxygen-content dependence of the CBM and VBM energies of $LaH_{3-2x}O_x$ (x = 0, 0.1, and 0.2). As the oxygen content increases, the band gap widens, primarily because the La-5d-derived CBM shifts upward, whereas the VBM slightly shifts downward. Consequently, the E_F, which lies at nearly the same energy relative to the $E_{vac.}$, moves toward the middle of the gap. This trend is consistent with the oxygen-content dependence of the observed electrical characteristics: LaH_3 behaves as an n-type electronic conductor,[53] while in the oxyhydrides, electronic conduction is suppressed and ion conduction becomes predominant.[34,35] The upward shift of the CBM with increasing oxygen content reflects the formation of La−O ionic bonds. This is supported by the core-level X-ray photoemission spectra for La 3d, which exhibit a downward shift relative to the $E_{vac.}$ with increasing oxygen content (Figure S7). On the other hand, the insensitivity of VBM energy to oxygen content suggests that the bonding character of La−H, and thus the nature of hydride ions, is not substantially altered by oxygen doping. Oxygen-undoped LaH_3 adopts a structure in which hydrogen densely occupies both the tetrahedral and octahedral interstitial sites of the fcc La lattice. As a result, hydride ions in LaH_3 exhibit appreciable H−H interactions, and the VBM is dominated by the antibonding states between neighboring hydride ions, which significantly elevate the VBM relative to the energy of isolated hydride ions. Consequently, the H 1s-derived VBM lies close to the E_F, indicating that hydride ions in LaH_3 are

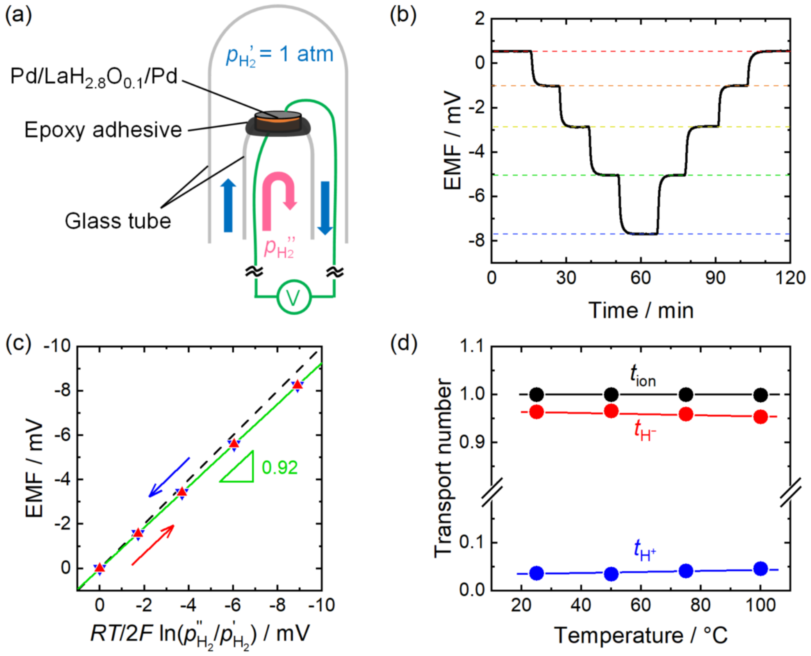

Figure 5. EMF measurements of a hydrogen concentration cell. (a) Schematic illustration of the hydrogen concentration cell setup for $LaH_{2.8}O_{0.1}$. (b) Time evolution of the EMF at 25 °C when p'_{H_2} is fixed at 1 atm while p''_{H_2} is varied. The dashed lines in red, orange, yellow, green, and blue serve as eye guides for p''_{H_2} = 1.0, 0.88, 0.75, 0.63, and 0.50 atm, respectively. (c) EMF at 25 °C plotted as a function of $\frac{RT}{2F}\ln(p''_{H_2}/p'_{H_2})$. The red triangles denote the EMF values obtained while p''_{H_2} is decreased, whereas the blue triangles denote those obtained while p''_{H_2} is increased. The corresponding linear fit, shown as a green line, and slope are also presented. The black dashed line represents a slope of 1. (d) Temperature dependence of the apparent transport numbers of H^- (red) and H^+ (blue) determined from the EMF measurements, together with the ionic transport number from the DC polarization of a Mo ion-blocking cell (black).

better described as being close to a neutral hydrogen than those in ionic alkali and alkaline-earth metal hydrides.[51,54] These characteristic features of hydride ions are largely retained in the oxygen-doped oxyhydrides.

Figure 4a plots the calculated defect formation energies of point defects against the E_F in $LaH_{2.5}O_{0.5}$ under $p_{H_2} = 1$ atm at 300 K. As demonstrated in Figures 2b, S8, and S9, $LaH_{3-2x}O_x$ can switch between ionic and electronic conductive states by the electrochemical insertion and extraction of H^- and variations in p_{H_2} or μ_H in the gas phase. In the temperature range of our experiments (≤100 °C), only hydrogen species exhibit appreciable mobility, whereas La and O are essentially immobile.[35] Accordingly, the equilibrium E_F was estimated by imposing charge neutrality on the defects whose formation does not involve La or O diffusion. Under $p_{H_2} = 1$ atm or $\mu_H = \mu_H^\circ$, the equilibrium E_F is determined by charge compensation between positively charged $V_{H(Oc.)}^\bullet$ and negatively charged $O_{H(T)}'$ and H_i'. Here, the interstitial site is an octahedral anion site that is left vacant upon oxygen substitution to maintain charge neutrality. The resultant E_F lies approximately 0.6 eV below the CBM, which is in good agreement with the experimentally observed energy separation between the E_F and CBM in $LaH_{2.6}O_{0.2}$ shown in Figure 3.

Under $p_{H_2} \gg 1$ atm or $\mu_H \gg \mu_H^\circ$, $V_{H(Oc.)}$ formation becomes less favorable, whereas H_i formation becomes more favorable. Consequently, the E_F, which is determined by the charge neutrality between these defects, shifts to a lower level. This trend is confirmed by calculations at $p_{H_2} = 100$ atm, as shown in Figure S10. Thus, upon anodic polarization, as shown in Figure 2b, provided that polarization is not limited by the H_2 evolution reaction, the E_F can be lowered to the charge neutrality level (CNL), ε (±), of H_i[22,26] and does not decrease further because it is pinned at the CNL by the redox equilibrium between negatively charged H_i' and positively charged $H_i^\bullet$. For this reason, E_F never drops into the valence band, and the hole-doping reaction described by eq 3, in which $H_i^\times$ acts as an acceptor, does not occur. Even when a more positive potential is applied beyond this CNL to further lower the E_F, H_i is oxidized according to eq 4, generating electrons. The released electrons populate an impurity band in the gap, leading to electronic conduction, as observed upon anodic polarization of the oxyhydride (Figure 2b). The impurity band formed during this process may be analogous to that generated by the photoinduced protonation of H^- in rare-earth oxyhydride thin films, a process proposed as the origin of their photochromic behavior.[55,56] Electronic conduction is observed upon only a slight anodic polarization with respect to the Pd electrode equilibrated with 1 atm of H_2. This finding suggests that the experimental E_F in equilibrium with the hydrogen atmosphere is located very close to the CNL of H_i, which represents the oxidation limit of H^-.

The relaxed structures of $LaH_{2.5}O_{0.5}$ containing H_i' and $H_i^\bullet$ are presented in Figure 4c,d, respectively. $H_i^\bullet$ is electrostatically attracted to hydrogen at the nearest tetrahedral site, and a dihydrogen defect, which can be denoted as $H_{2i}^\bullet$ in Kröger–Vink notation, is formed. The resulting H–H distance of 0.84 Å is significantly longer than that in a H_2 molecule (0.74 Å).[57] Such a dihydrogen defect may be regarded as analogous to that in transition-metal dihydrogen complexes in organometallic chemistry.[58] In these complexes, an H_2 molecule can bind side-on to the metal center by donating its two σ electrons to a vacant metal d orbital. The elongated H−H bond observed in $LaH_{2.5}O_{0.25}$ is attributable to bonding interactions with the neighboring La cations, as indicated by the red dashed line in Figure 4d. A similar configuration has been reported for crystalline yttrium oxyhydrides, $YH_{3-2x}O_x$, in relation to their photochromic mechanism, in which such dihydrogen defects have been proposed to act as electron donors.[56,59]

Our static DFT calculations indicate that the formation energy of $H_i^\bullet$ is rather larger than that of $V_{H(Oc.)}^\bullet$, implying that $H_i^\bullet$ is unlikely to contribute to determining the E_F position under $p_{H_2} = 1$ atm at 300 K. This assessment, however, does not fully reflect the actual hydrogen environment in $LaH_{3-2x}O_x$. As described above, in $LaH_{3-2x}O_x$, most of the tetrahedral and octahedral interstitial sites of the fcc La sublattice are occupied by hydrogen, resulting in a densely packed hydrogen sublattice. In such an environment, H_i can readily engage in bonding−antibonding interactions with the surrounding H^-, giving rise to a shift in the CNL to higher energies, thereby making H_i' more susceptible to oxidation and lowering the formation energy of $H_i^\bullet$ (Figure 4e). This is reasonable in light of the fact that hydrogen exhibits high diffusivity in $LaH_{3-2x}O_x$ even at room temperature. Under such conditions, the positive charge need not remain statically localized within a single H−H pair but can be shared by a larger number of surrounding mobile H^-. Such collective interactions within the hydrogen network stabilize $H_i^\bullet$ compared with the static-defect picture. As a consequence, $LaH_{3-2x}O_x$ is expected to exhibit a characteristic high CNL, which narrows the oxidizing limit of the ECW. Accordingly, at equilibrium under $p_{H_2} = 1$ atm, E_F is located just above the elevated CNL, so that a slight anodic polarization, corresponding to a small downward shift of E_F, would be sufficient to reach the CNL.

The EMF of a hydrogen concentration cell was measured under conditions near 1 atm of H_2 using the experimental setup illustrated in Figure 5a. A symmetric Pd/$LaH_{2.8}O_{0.1}$/Pd cell was bonded to a Pyrex tube with epoxy adhesive, which served as a gastight seal separating the two electrodes. The cross-sectional scanning electron microscopy image of $LaH_{2.8}O_{0.1}$ in Figure S2 reveals a dense microstructure without observable voids, indicating that mechanical gas leakage through the pellet is negligible when a hydrogen partial-pressure gradient is applied across the sample.

Figure 5b shows the EMF relaxation behavior recorded at 25 °C following stepwise changes in the hydrogen partial pressure, p''_{H_2}, at one electrode, while the hydrogen partial pressure at the other electrode, p'_{H_2}, was fixed at 1 atm. Owing to the bipolarity of hydrogen, two types of electrode reactions can be considered

$$\frac{1}{2}H_2 = H^+ + e^- \tag{5}$$

and

$$\frac{1}{2}H_2 + e^- = H^- \tag{6}$$

The corresponding theoretical magnitudes of the EMF for these reactions are given by eqs 7 and 8, respectively.

$$\mathrm{EMF}_{H^+} = -t_{H^+}\frac{RT}{2F}\ln(p''_{H_2}/p'_{H_2}) \tag{7}$$

$$\mathrm{EMF}_{H^-} = t_{H^-}\frac{RT}{2F}\ln(p''_{H_2}/p'_{H_2}) \tag{8}$$

where t_{H^+} and t_{H^-} are the transport numbers of H^+ and H^-, respectively. Thus, the negative EMF on the lower p''_{H_2} side clearly indicates that eq 6 is dominant for Pd/$LaH_{2.8}O_{0.1}$. The EMF exhibits fast relaxation and attains a steady state within ∼10 min, indicating that the electrode reactions have reached equilibrium. This is attributed to rapid H_2 dissociation and association at Pd electrodes.

As shown in Figure 5c, the measured EMF is proportional to $\frac{RT}{2F}\ln(p''_{H_2}/p'_{H_2})$, but its magnitude is slightly smaller than the value for $t_{H^-} = 1$, indicating that t_{H^-} is somewhat less than 1. However, as shown in Figure S5, under these conditions, the transport number of electronic carriers t_{el} is very small ($<10^{-4}$), and t_{ion} is essentially 1. Thus, the reduced EMF cannot be ascribed to electronic leakage.

Considering that the EMF is measured under conditions in which H_i can be partially protonated, the EMF may be expected to include contributions from not only the reaction described by eq 8 but also that described by eq 7. The EMF determined by the competition between these reactions is given by eq 9

$$\mathrm{EMF} = \frac{RT}{2F}(t_{H^-} - t_{H^+})\ln(p''_{H_2}/p'_{H_2}) \tag{9}$$

The slope of the experimental EMF in Figure 5c corresponds to the value of $t_{H^-} - t_{H^+}$. The apparent individual values of t_{H^-} and t_{H^+} can be determined using $t_{ion} = t_{H^-} + t_{H^+} = 1$, as summarized in Figure 5d. We emphasize that the EMF data only quantify the net number of charges transported per hydrogen transported and, therefore, do not identify the microscopic mechanism of the mixed conduction of H^- and H^+. Nevertheless, the observed EMF behavior suggests that, as discussed above, the E_F approaches the CNL of the H_i under a H_2 atmosphere.

Here, we take an overview of the amphoteric behavior of hydrogen across H^+ and H^- conductors from the perspective of an electronic energy scale. Figure 6 summarizes the energy band alignments of $LaH_{3-2x}O_x$ (left) and a typical perovskite-type proton-conducting oxide electrolyte, that is, an acceptor-doped $BaZrO_3$ (Acc-doped BZO; right).[60] The ECW of $LaH_{3-2x}O_x$ is also shown, and all energy levels are referenced

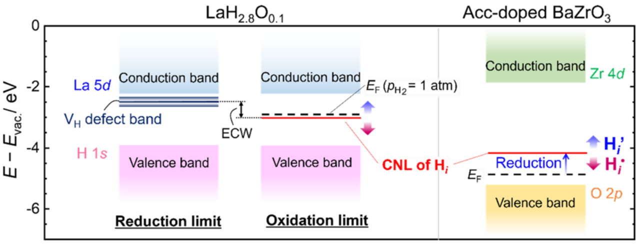

Figure 6. Energy band alignments of $LaH_{2.8}O_{0.1}$ and a proton-conducting acceptor-doped $BaZrO_3$ (Acc-doped BZO), together with the electrochemical window (ECW). The band positions and ECW of $LaH_{2.8}O_{0.1}$ were determined experimentally in this work. The band alignment of Acc-doped BZO was constructed based on values reported in previous studies,[60] with the E_F drawn schematically at an arbitrary level below the midgap under oxidizing conditions. Upon reduction of Acc-doped BZO, the E_F shifts toward the CNL of H_i, leading to the conversion of H^+ into H^-.

to the $E_{vac.}$. At the reduction limit of $LaH_{3-2x}O_x$ (i.e., low p_{H_2}), $V_H^{\bullet}$ formation gives rise to a defect band just below the conduction band. At the oxidation limit (i.e., high p_{H_2}), H_i oxidation leads to electron doping. Thus, the CNL of the H_i corresponds to this oxidation limit. The E_F of $LaH_{3-2x}O_x$ in equilibrium with 1 atm of H_2 lies close to this oxidation limit. As revealed by the EMF measurements, hydrogen transport under these conditions involves not only H^- conduction but also a partial contribution from H^+ conduction. However, because the E_F remains within the ECW, $LaH_{3-2x}O_x$ does not exhibit electronic conduction.

The VBM of Acc-doped BZO, which is mainly composed of O 2*p* states, lies nearly 2 eV lower in energy than the H 1*s*-derived VBM of $LaH_{3-2x}O_x$. In Acc-doped BZO, oxygen vacancies ($V_O^{\bullet\bullet}$) form to maintain charge neutrality upon acceptor doping. Protons are introduced via the hydration reaction of $V_O^{\bullet\bullet}$ and conduct as ionic charge carriers.[9] As the E_F of Acc-doped BZO is located closer to the VBM than to the middle of the band gap under oxidizing conditions,[61] this E_F is positioned at a significantly lower energy than that of $LaH_{3-2x}O_x$, illustrating that $LaH_{3-2x}O_x$ has much stronger reducing power than proton-conducting oxides such as Acc-BZO.[19]

Under strongly reducing conditions, perovskite-type oxides can accommodate H^-, leading to mixed H^- and electronic conduction.[6,18,32] This may be understood as the E_F crossing the CNL of H_i from the oxidizing to the reducing side, thereby changing from H^+ to H^-. Thus, the CNL of H_i defines the reducing limit of Acc-doped BZO. To the best of our knowledge, however, the reduction behavior of these oxides has not yet been examined in terms of electronic energy on an absolute scale referenced to the $E_{vac.}$. Nevertheless, theoretical calculations indicate that, among various oxides, the CNL of H_i is typically located at around −4 eV relative to the $E_{vac.}$.[24−26] This provides a clear contrast to $LaH_{3-2x}O_x$, in which the CNL is located at an exceptionally high energy owing to strong H−H interactions.

Taken together, it can be seen that, among materials that accommodate what are referred to as "hydride ions", the position of the E_F can vary widely. Although "hydride ions" are commonly regarded as strong reducing species based on an electrode potential of $E(H_2/H^-) = -2.25$ V versus the standard hydrogen electrode in aqueous systems,[62] the fact that their redox potential in solids, $E(H^+/H^-)$—corresponding to the CNL position—is strongly dependent on the host material has largely been overlooked. Describing hydrogen in solids in terms of an electronic energy scale is expected to provide valuable insight into its chemical reactivity and charge-transport properties. Future studies that systematically organize band alignments across a wide range of hydrogen-ion conductors will help achieve a comprehensive understanding of the characteristics of hydrogen in solids and will provide a rational basis for designing new electrochemical devices that exploit the amphoteric nature of hydrogen.

■ CONCLUSION

In this work, we investigated the ECW of $LaH_{3-2x}O_x$ and positioned it on an absolute electronic energy scale referenced to the $E_{vac.}$. The ECW of the $LaH_{2.8}O_{0.1}$ thin film determined by Hebb−Wagner polarization ranged from approximately −0.4 to 0 V versus Pd in equilibrium with a 1 atm H_2 atmosphere. From the photoemission experiments, we determined the positions of the VBM and CBM of $LaH_{3-2x}O_x$ (x = 0, 0.1, and 0.2) from the $E_{vac.}$; the VBM lies at approximately −4 eV, while the CBM is located at −2.5 to −2 eV, depending on the oxygen content of the oxyhydride. We found that the E_F under 1 atm of H_2 is determined by the charge neutrality condition among H_i', $V_H^{\bullet}$, and O_H', and lies above the midgap, close to the CBM. Based on this E_F position, we examined the redox reactions that determine the reducing and oxidizing limits of the ECW of $LaH_{3-2x}O_x$. The reducing limit of the ECW is governed by the hydrogen extraction reaction from $LaH_{3-2x}O_x$, which creates $V_H^{\bullet}$ and thereby forms a defect band near the CBM, giving rise to electronic conduction. On the other hand, the oxidizing limit of the ECW is not governed by H_2 evolution from the oxidation of H^- but by a reaction in which interstitial H^- ions capture positive charges to form H^+, thereby giving rise to electronic conduction. This implies that the E_F approaches the CNL of H_i. H^+ can be stabilized in the H^- lattice through bonding−antibonding interactions with the surrounding H^- ions, enabled by the short H−H separations in $LaH_{3-2x}O_x$. When the EMF of a hydrogen concentration cell is measured near p_{H_2} = 1 atm, which is close to the onset of H_i oxidation, both H^- conduction and a partial contribution from H^+ conduction are observed. Such behavior reflects the amphoteric nature of hydrogen. Capturing this amphoteric nature of hydrogen on an electronic energy scale provides a unified perspective on the chemical reactivity and charge-transport properties across different classes of hydrogen-ion conductors. Our findings can contribute to the rational design and understanding of new materials and devices that effectively exploit the amphoteric character of hydrogen.

■ ASSOCIATED CONTENT

Supporting Information

The Supporting Information is available free of charge at https://pubs.acs.org/doi/10.1021/jacs.6c01849.

Details of structural and compositional analyses for prepared $LaH_{3-2x}O_x$, UPS spectra of $LaH_{2.8}O_{0.1}$ thin films, mechanical failure induced by hydrogen evolution at the Mo/$LaH_{2.8}O_{0.1}$ interface, ion blocking measurements for $LaH_{2.8}O_{0.1}$, XPS spectra of $LaH_{3-2x}O_x$, electrical properties of $LaH_{2.6}O_{0.2}$ dependent on the hydrogen chemical potential in the atmosphere, and calculated defect formation energy in $LaH_{2.5}O_{0.25}$ (PDF)

■ AUTHOR INFORMATION

Corresponding Author

Tomoyuki Yamasaki − *Institute of Multidisciplinary Research for Advanced Materials (IMRAM), Tohoku University, Sendai 980-8577, Japan*; orcid.org/0000-0002-6982-7538; Email: tomoyuki.yamasaki.a1@tohoku.ac.jp

Authors

Keiga Fukui − *Graduate Faculty of Interdisciplinary Research, University of Yamanashi, Kofu, Yamanashi 400-8511, Japan*; orcid.org/0000-0002-5659-7200
Soshi Iimura − *National Institute for Materials Science (NIMS), Tsukuba, Ibaraki 305−0047, Japan*
Shunsuke Tsuda − *National Institute for Materials Science (NIMS), Tsukuba, Ibaraki 305−0047, Japan*

Hiroshi Mizoguchi − *National Institute for Materials Science (NIMS), Tsukuba, Ibaraki 305−0047, Japan;* orcid.org/0000-0002-0992-7449

Takahisa Omata − *Institute of Multidisciplinary Research for Advanced Materials (IMRAM), Tohoku University, Sendai 980-8577, Japan;* orcid.org/0000-0002-6034-4935

Hideo Hosono − *National Institute for Materials Science (NIMS), Tsukuba, Ibaraki 305−0047, Japan; International Research Frontiers initiative MDX Research Center for Element Strategy, Institute of Science Tokyo, Yokohama 226−8503, Japan*

Complete contact information is available at: https://pubs.acs.org/10.1021/jacs.6c01849

Notes

The authors declare no competing financial interest.

■ ACKNOWLEDGMENTS

This work was supported by the MEXT Element Strategy Initiative to Form Core Research Center (Grant Number JPMXP0112101001). T.Y. was supported in part by JSPS KAKENHI (Grant Numbers 23K19174 and 24K17762). This work was also partly supported by the Material Solutions Center (MaSC), Tohoku University, Japan.

■ REFERENCES

(1) Huiberts, J. N.; Griessen, R.; Rector, J. H.; Wijngaarden, R. J.; Dekker, J. P.; de Groot, D. G.; Koeman, N. J. Yttrium and Lanthanum Hydride Films with Switchable Optical Properties. *Nature* **1996**, *380* (6571), 231−234.

(2) Hayashi, K.; Matsuishi, S.; Kamiya, T.; Hirano, M.; Hosono, H. Light-Induced Conversion of an Insulating Refractory Oxide into a Persistent Electronic Conductor. *Nature* **2002**, *419* (6906), 462−465.

(3) Mongstad, T.; Platzer-Björkman, C.; Maehlen, J. P.; Mooij, L. P. A.; Pivak, Y.; Dam, B.; Marstein, E. S.; Hauback, B. C.; Karazhanov, S. Zh. A New Thin Film Photochromic Material: Oxygen-Containing Yttrium Hydride. *Sol. Energy Mater. Sol. Cells* **2011**, *95* (12), 3596−3599.

(4) Hayward, M. A.; Cussen, E. J.; Claridge, J. B.; Bieringer, M.; Rosseinsky, M. J.; Kiely, C. J.; Blundell, S. J.; Marshall, I. M.; Pratt, F. L. The Hydride Anion in an Extended Transition Metal Oxide Array: $LaSrCoO_3H_{0.7}$. *Science* **2002**, *295* (5561), 1882−1884.

(5) Montero, J.; Svedlindh, P.; Österlund, L. Photo-Induced Reversible Modification of the Curie−Weiss Temperature in Paramagnetic Gadolinium Compounds. *Solid State Commun.* **2024**, *378*, No. 115419.

(6) Kobayashi, Y.; Hernandez, O. J.; Sakaguchi, T.; Yajima, T.; Roisnel, T.; Tsujimoto, Y.; Morita, M.; Noda, Y.; Mogami, Y.; Kitada, A.; Ohkura, M.; Hosokawa, S.; Li, Z.; Hayashi, K.; Kusano, Y.; Kim, J. eun.; Tsuji, N.; Fujiwara, A.; Matsushita, Y.; Yoshimura, K.; Takegoshi, K.; Inoue, M.; Takano, M.; Kageyama, H. An Oxyhydride of $BaTiO_3$ Exhibiting Hydride Exchange and Electronic Conductivity. *Nat. Mater.* **2012**, *11* (6), 507−511.

(7) Bang, J.; Matsuishi, S.; Hiraka, H.; Fujisaki, F.; Otomo, T.; Maki, S.; Yamaura, J.; Kumai, R.; Murakami, Y.; Hosono, H. Hydrogen Ordering and New Polymorph of Layered Perovskite Oxyhydrides: $Sr_2VO_{4-x}H_x$. *J. Am. Chem. Soc.* **2014**, *136* (20), 7221−7224.

(8) Takagi, S.; Orimo, S. Recent Progress in Hydrogen-Rich Materials from the Perspective of Bonding Flexibility of Hydrogen. *Scr. Mater.* **2015**, *109*, 1−5.

(9) Kreuer, K. D. Proton-Conducting Oxides. *Annu. Rev. Mater. Res.* **2003**, *33* (33, 2003), 333−359.

(10) Tsujikawa, K.; Hyodo, J.; Fujii, S.; Takahashi, K.; Tomita, Y.; Shi, N.; Murakami, Y.; Kasamatsu, S.; Yamazaki, Y. Mitigating Proton Trapping in Cubic Perovskite Oxides via ScO_6 Octahedral Networks. *Nat. Mater.* **2025**, *24*, 1949−1956.

(11) Haile, S. M.; Chisholm, C. R. I.; Sasaki, K.; Boysen, D. A.; Uda, T. Solid Acid Proton Conductors: From Laboratory Curiosities to Fuel Cell Electrolytes. *Faraday Discuss.* **2007**, *134* (0), 17−39.

(12) Fop, S.; Vivani, R.; Masci, S.; Casciola, M.; Donnadio, A. Anhydrous Superprotonic Conductivity in the Zirconium Acid Triphosphate $ZrH_5(PO_4)_3$. *Angew. Chem., Int. Ed.* **2023**, *62* (18), No. e202218421.

(13) Yamaguchi, T.; Tsukuda, S.; Ishiyama, T.; Nishii, J.; Yamashita, T.; Kawazoe, H.; Omata, T. Proton-Conducting Phosphate Glass and Its Melt Exhibiting High Electrical Conductivity at Intermediate Temperatures. *J. Mater. Chem. A* **2018**, *6* (46), 23628−23637.

(14) Verbraeken, M. C.; Cheung, C.; Suard, E.; Irvine, J. T. S. High H− Ionic Conductivity in Barium Hydride. *Nat. Mater.* **2015**, *14* (1), 95−100.

(15) Papac, M.; Stevanović, V.; Zakutayev, A.; O'Hayre, R. Triple Ionic−Electronic Conducting Oxides for next-Generation Electrochemical Devices. *Nat. Mater.* **2021**, *20* (3), 301−313.

(16) Shiraiwa, T.; Yamasaki, T.; Kushimoto, K.; Kano, J.; Omata, T. Enhanced Proton Transport in Nb-Doped Rutile TiO_2: A Highly Useful Class of Proton-Conducting Mixed Ionic Electronic Conductors. *J. Am. Chem. Soc.* **2025**, *147* (34), 30757−30767.

(17) Kura, C.; Kunisada, Y.; Tsuji, E.; et al. Hydrogen Separation by Nanocrystalline Titanium Nitride Membranes with High Hydride Ion Conductivity. *Nat. Energy* **2017**, *2*, 786−794.

(18) Toriumi, H.; Kobayashi, G.; Saito, T.; Kamiyama, T.; Sakai, T.; Nomura, T.; Kitano, S.; Habazaki, H.; Aoki, Y. Barium Indate−Zirconate Perovskite Oxyhydride with Enhanced Hydride Ion/Electron Mixed Conductivity. *Chem. Mater.* **2022**, *34* (16), 7389−7401.

(19) Ooya, K.; Li, J.; Fukui, K.; Iimura, S.; Nakao, T.; Ogasawara, K.; Sasase, M.; Abe, H.; Niwa, Y.; Kitano, M.; Hosono, H. Ruthenium Catalysts Promoted by Lanthanide Oxyhydrides with High Hydride-Ion Mobility for Low-Temperature Ammonia Synthesis. *Adv. Energy Mater.* **2021**, *11* (4), No. 2003723.

(20) Clark, D.; Malerød-Fjeld, H.; Budd, M.; Yuste-Tirados, I.; Beeaff, D.; Aamodt, S.; Nguyen, K.; Ansaloni, L.; Peters, T.; Vestre, P. K.; Pappas, D. K.; Valls, M. I.; Remiro-Buenamañana, S.; Norby, T.; Bjørheim, T. S.; Serra, J. M.; Kjølseth, C. Single-Step Hydrogen Production from NH_3, CH_4, and Biogas in Stacked Proton Ceramic Reactors. *Science* **2022**, *376* (6591), 390−393.

(21) Hirose, T.; Matsui, N.; Itoh, T.; Hinuma, Y.; Ikeda, K.; Gotoh, K.; Jiang, G.; Suzuki, K.; Hirayama, M.; Kanno, R. High-Capacity, Reversible Hydrogen Storage Using H−-Conducting Solid Electrolytes. *Science* **2025**, *389* (6766), 1252−1255.

(22) Van de Walle, C. G.; Neugebauer, J. HYDROGEN IN SEMICONDUCTORS. *Annu. Rev. Mater. Res.* **2006**, *36* (1), 179−198.

(23) McCluskey, M. D.; Tarun, M. C.; Teklemichael, S. T. Hydrogen in Oxide Semiconductors. *J. Mater. Res.* **2012**, *27* (17), 2190−2198.

(24) Kılıç, Ç.; Zunger, A. N-Type Doping of Oxides by Hydrogen. *Appl. Phys. Lett.* **2002**, *81* (1), 73−75.

(25) Van de Walle, C. G.; Neugebauer, J. Universal Alignment of Hydrogen Levels in Semiconductors, Insulators and Solutions. *Nature* **2003**, *423* (6940), 626−628.

(26) Kadono, R.; Hosono, H. Ambipolarity of Hydrogen in Matter Revealed by Muons. *Adv. Phys.* **2023**, *72* (4), 409−476.

(27) Chaykina, D.; de Krom, T.; Colombi, G.; Schreuders, H.; Suter, A.; Prokscha, T.; Dam, B.; Eijt, S. Structural Properties and Anion Dynamics of Yttrium Dihydride and Photochromic Oxyhydride Thin Films Examined by *in Situ* μ^+ SR. *Phys. Rev. B* **2021**, *103* (22), No. 224106.

(28) Bai, C.; Li, Y.; Xiao, G.; Chen, J.; Tan, S.; Shi, P.; Hou, T.; Liu, M.; He, Y.-B.; Kang, F. Understanding the Electrochemical Window of Solid-State Electrolyte in Full Battery Application. *Chem. Rev.* **2025**, *125* (14), 6541−6608.

(29) Thompson, T.; Yu, S.; Williams, L.; Schmidt, R. D.; Garcia-Mendez, R.; Wolfenstine, J.; Allen, J. L.; Kioupakis, E.; Siegel, D. J.;

Sakamoto, J. Electrochemical Window of the Li-Ion Solid Electrolyte $Li_7La_3Zr_2O_{12}$. *ACS Energy Lett.* **2017**, *2* (2), 462−468.

(30) Tateyama, Y.; Gao, B.; Jalem, R.; Haruyama, J. Theoretical Picture of Positive Electrode−Solid Electrolyte Interface in All-Solid-State Battery from Electrochemistry and Semiconductor Physics Viewpoints. *Curr. Opin. Electrochem.* **2019**, *17*, 149−157.

(31) Hikima, K.; Shimizu, K.; Kiuchi, H.; Hinuma, Y.; Suzuki, K.; Hirayama, M.; Matsubara, E.; Kanno, R. Operando Analysis of Electronic Band Structure in an All-Solid-State Thin-Film Battery. *Commun. Chem.* **2022**, *5* (1), No. 52.

(32) Takahashi, T.; Toriumi, H.; Kobayashi, G.; Saito, T.; Mori, K.; Jeong, S.; Habazaki, H.; Aoki, Y. Mechanistic Insights into Hydride Incorporation in $BaZr_{1-x}In_xO_{3-\delta}$-Based Perovskite Oxyhydrides. *Chem. Mater.* **2025**, *37* (19), 7834−7845.

(33) Maeda, R.; Toriumi, H.; Takahashi, T.; Ariga-Miwa, H.; Uruga, T.; Jeong, S.; Aoki, Y. Bipolar Electrolysis Cells with Hydride Ion-Proton Conductor Heterojunctions. *Cell Rep. Phys. Sci.* **2025**, *6* (10), No. 102839.

(34) Fukui, K.; Iimura, S.; Tada, T.; Fujitsu, S.; Sasase, M.; Tamatsukuri, H.; Honda, T.; Ikeda, K.; Otomo, T.; Hosono, H. Characteristic Fast H^- Ion Conduction in Oxygen-Substituted Lanthanum Hydride. *Nat. Commun.* **2019**, *10* (1), No. 2578.

(35) Fukui, K.; Iimura, S.; Iskandarov, A.; Tada, T.; Hosono, H. Room-Temperature Fast H^- Conduction in Oxygen-Substituted Lanthanum Hydride. *J. Am. Chem. Soc.* **2022**, *144* (4), 1523−1527.

(36) Abdellah, A. M.; Ismail, F.; Siig, O. W.; Yang, J.; Andrei, C. M.; DiCecco, L.-A.; Rakhsha, A.; Salem, K. E.; Grandfield, K.; Bassim, N.; Black, R.; Kastlunger, G.; Soleymani, L.; Higgins, D. Impact of Palladium/Palladium Hydride Conversion on Electrochemical CO_2 Reduction via in-Situ Transmission Electron Microscopy and Diffraction. *Nat. Commun.* **2024**, *15* (1), No. 938.

(37) Guo, J.; Cai, Y.; Gao, W.; Chen, P. Hydrides for Dinitrogen Conversion. *ACS Catal.* **2025**, *15* (17), 14805−14812.

(38) Yamasaki, T.; Takaoka, R.; Iimura, S.; Kim, J.; Hiramatsu, H.; Hosono, H. Characteristic Resistive Switching of Rare-Earth Oxyhydrides by Hydride Ion Insertion and Extraction. *ACS Appl. Mater. Interfaces* **2022**, *14* (17), 19766−19773.

(39) Kresse, G.; Furthmüller, J. Efficient Iterative Schemes for Ab Initio Total-Energy Calculations Using a Plane-Wave Basis Set. *Phys. Rev. B* **1996**, *54* (16), 11169−11186.

(40) Kresse, G.; Furthmüller, J. Efficiency of Ab-Initio Total Energy Calculations for Metals and Semiconductors Using a Plane-Wave Basis Set. *Comput. Mater. Sci.* **1996**, *6* (1), 15−50.

(41) Perdew, J. P.; Burke, K.; Ernzerhof, M. Generalized Gradient Approximation Made Simple. *Phys. Rev. Lett.* **1996**, *77* (18), No. 3865.

(42) Kresse, G.; Joubert, D. From Ultrasoft Pseudopotentials to the Projector Augmented-Wave Method. *Phys. Rev. B* **1999**, *59* (3), No. 1758.

(43) Colombi, G.; Stigter, R.; Chaykina, D.; Banerjee, S.; Kentgens, A. P. M.; Eijt, S. W. H.; Dam, B.; de Wijs, G. A. Energy, Metastability, and Optical Properties of Anion-Disordered RO_xH_{3-2x} (Y, La) Oxyhydrides: A Computational Study. *Phys. Rev. B* **2022**, *105* (5), No. 054208.

(44) Kumagai, Y.; Tsunoda, N.; Takahashi, A.; Oba, F. Insights into Oxygen Vacancies from High-Throughput First-Principles Calculations. *Phys. Rev. Mater.* **2021**, *5* (12), No. 123803.

(45) Nakatsuji, H.; Hada, M. Interaction of a Hydrogen Molecule with Palladium. *J. Am. Chem. Soc.* **1985**, *107* (26), 8264−8266.

(46) Flanagan, T. B.; Oates, W. A. The Palladium-Hydrogen System. *Annu. Rev. Mater. Res.* **1991**, *21*, 269−304.

(47) Lin, D.; Lasia, A. Electrochemical Impedance Study of the Kinetics of Hydrogen Evolution at a Rough Palladium Electrode in Acidic Solution. *J. Electroanal. Chem.* **2017**, *785*, 190−195.

(48) Maier, J. *Physical Chemistry of Ionic Materials: Ions and Electrons in Solids*; John Wiley & Sons, 2004.

(49) Kröger, F.; Vink, H. J. Relations between the Concentrations of Imperfections in Solids. *J. Phys. Chem. Solids* **1958**, *5* (3), 208−223.

(50) Ng, K. K.; Zhang, F. C.; Anisimov, V. I.; Rice, T. M. Theory for Metal Hydrides with Switchable Optical Properties. *Phys. Rev. B* **1999**, *59* (8), No. 5413.

(51) Yamasaki, T.; Iimura, S.; Kim, J.; Hosono, H. Extremely Shallow Valence Band in Lanthanum Trihydride. *J. Am. Chem. Soc.* **2023**, *145* (1), 560−566.

(52) Yeh, J. J.; Lindau, I. Atomic Subshell Photoionization Cross Sections and Asymmetry Parameters: $1 \leqslant Z \leqslant 103$. *At. Data Nucl. Data Tables* **1985**, *32* (1), 1−155.

(53) Libowitz, G. G. Electronic Properties of the Rare Earth Hydrides. *Ber. Bunsengesellschaft Phys. Chem.* **1972**, *76* (8), 837−845.

(54) Misemer, D. K.; Harmon, B. N. Self-Consistent Electronic Structure of Lanthanum Dihydride and Lanthanum Trihydride. *Phys. Rev. B* **1982**, *26* (10), No. 5634.

(55) Komatsu, Y.; Shimizu, R.; Sato, R.; Wilde, M.; Nishio, K.; Katase, T.; Matsumura, D.; Saitoh, H.; Miyauchi, M.; Adelman, J. R.; McFadden, R. M. L.; Fujimoto, D.; Ticknor, J. O.; Stachura, M.; McKenzie, I.; Morris, G. D.; MacFarlane, W. A.; Sugiyama, J.; Fukutani, K.; Tsuneyuki, S.; Hitosugi, T. Repeatable Photoinduced Insulator-to-Metal Transition in Yttrium Oxyhydride Epitaxial Thin Films. *Chem. Mater.* **2022**, *34* (8), 3616−3623.

(56) Banerjee, S.; Chaykina, D.; Stigter, R.; Colombi, G.; Eijt, S. W. H.; Dam, B.; de Wijs, G. A.; Kentgens, A. P. M. Exploring Multi-Anion Chemistry in Yttrium Oxyhydrides: Solid-State NMR Studies and DFT Calculations. *J. Phys. Chem. C* **2023**, *127* (29), 14303−14316.

(57) Huber, K. P.; Herzberg, G. Constants of Diatomic Molecules. In *Molecular Spectra and Molecular Structure: IV. Constants of Diatomic Molecules*; Huber, K. P.; Herzberg, G., Eds.; Springer US: Boston, MA, 1979; pp 8−689 DOI: 10.1007/978-1-4757-0961-2_2.

(58) Kubas, G. J. Fundamentals of H_2 Binding and Reactivity on Transition Metals Underlying Hydrogenase Function and H_2 Production and Storage. *Chem. Rev.* **2007**, *107* (10), 4152−4205.

(59) Chai, J.; Shao, Z.; Wang, H.; Ming, C.; Oh, W.; Ye, T.; Zhang, Y.; Cao, X.; Jin, P.; Zhang, S.; Sun, Y.-Y. Ultrafast Processes in Photochromic Material YH_xO_y Studied by Excited-State Density Functional Theory Simulation. *Sci. China Mater.* **2020**, *63* (8), 1579−1587.

(60) Saeed, S. W.; Norby, T.; Bjørheim, T. S. Charge-Carrier Enrichment at $BaZrO_3/SrTiO_3$ Interfaces. *J. Phys. Chem. C* **2019**, *123* (34), 20808−20816.

(61) Rowberg, A. J. E.; Li, M.; Ogitsu, T.; Varley, J. B. Polarons and Electrical Leakage in $BaZrO_3$ and $BaCeO_3$. *Phys. Rev. Mater.* **2023**, *7* (1), No. 015402.

(62) Pourbaix, M.; Franklin, J. A. *Atlas of electrochemical equilibria in aqueous solutions*, 2nd ed.; National Association of Corrosion Engineers: Houston, TX, 1974.